私立東海大學

資訊工程與科學研究所

碩士論文

指導教授：黃育仁 博士

利用分水嶺演算法應用於抗核抗體之切割與分類

Outline Detection for the HEp-2 Cell in Indirect immunofluorescence Images Using Watershed Segmentation and Classification

研究生：鐘家偉

中 華 民 國 九 十 七 年 六 月

摘要

所謂抗核抗體(ANA)就是血中的抗體對抗細胞核內的抗原，意即對抗自己細胞核內抗原的自體抗體。這些自體抗體的存在，與各種不同的免疫疾病息息相關，對於診斷不同的風濕性疾病具有非常重要的意義，ANA 的檢查方法為一種間接免疫螢光法，此為利用一種培養細胞 HEp-2 的細胞株做為酵素基質，此細胞之細胞核大，易於觀看，是目前使用最廣的一種 ANA 檢驗方法，此方法迅速、簡單且敏感性高，幾乎取代過去所用狼瘡細胞檢查法(LE cell)，所以臨床上已成為診斷免疫風濕性疾病常見之檢查。

關於近年來間接抗體螢光染色 HEp-2 細胞的研究主要都是著重於對這些細胞作分類的研究，因為要分別這些抗核抗體不同種類的樣式需要有受過專業的訓練或是有經驗的專家和醫生才能夠分辨的出來，而且這種專家或是醫生其實人數是少量的，所以目標是想發展一個能夠幫助醫生作診斷的系統，也就是能夠自動對這些抗核抗體先作切割，然後再對這些切割出來的抗核抗體作正確的分類的系統。

本篇論文的切割方法是一個改良式的兩階層的分水嶺演算法，而這個方法總共對 2305 個抗核抗體細胞作實驗(包含 456 diffuse patterns, 417 peripheral patterns, 719 coarse speckled patterns, 55 fine speckled patterns, 517discrete speckled patterns and 141 nucleolar patterns)，而這些細胞是由 44 張間接抗體螢光染色影像上取得的，接下來再利用 Learning Vector Quantization (LVQ) 和 51 個特徵對 1036 個切割出來的細胞做分類。

關鍵字：分水嶺演算法、影像切割、抗核抗體、間接免疫螢光法、學習向量機

ABSTRACT

Rationale and Objectives: Indirect immunofluorescence (IIF) with HEp-2 cells has been used to detect antinuclear autoantibodies (ANA) for diagnosing systemic autoimmune diseases. An automatic inspection system for the ANA testing can be partitioned into HEp-2 cell detection, fluorescence pattern classification and computer aided diagnosis phases. The aim of this study is to develop an automatic segmentation scheme to sketch outlines of fluorescence cells for HEp-2 cell detection in the IIF images and fluorescence pattern classification.

Materials and Methods: In the proposed a two-staged segmentation method, the similarity-based watershed algorithm with marker techniques was performed to obtain the contour of each fluorescence cell. This study evaluated 2305 autoantibody fluorescence patterns from 44 IIF images that can be divided into six pattern categories (including 456 diffuse patterns, 417 peripheral patterns, 719 coarse speckled patterns, 55 fine speckled patterns, 517discrete speckled patterns and 141 nucleolar patterns). And fluorescence pattern classification method utilized learning vector quantization (LVQ) and 51 features to classify. It total experiment on 1036 cells (782 training data and 254 testing data).

Results: The sensitivity of the six patterns except for discrete speckled pattern was 86.8%, other patterns are among 94.7% to 100%. The total average sensitivity was 94.7%. In the classification simulation, the total average correct rate is 0.803.

Conclusions: This study proposed an automatic segmentation method for detecting outlines of fluorescence cells in IIF images and then the proposed classification method is performed to identify the different fluorescence patterns. The segmentation and classification result is satisfying for clinical applications.

Keywords: watershed transformation, image segmentation, antinuclear autoantibodies, immunofluorescence pattern, learning vector quantization

TABLE OF CONTENTS

LIST OF FIGURES

LIST OF TABLES

CHAPTER 1

INTRODUCTION

Indirect immunofluorescence (IIF) with HEp-2 cells is performed to detect antinuclear autoantibodies (ANA) in diagnosis of systemic autoimmune diseases[1]. The study about IIF with HEp-2 cells like [2-4]. The ANA testing allows to scan a broad range of autoantibody entities and to describe them by distinct fluorescence patterns. The fluorescence patterns are usually identified by physician manual inspecting the slides with the help of a microscope [5]. However, the inspection procedure still needs highly specialized and experienced technician or physician to obtain diagnostic result due to lacking in a low level of standardization and satisfied automation of inspection [6,7]. For this purpose, automatic inspection for fluorescence patterns in IIF image may assist physicians, without relevant experience, in making correct diagnosis. With ANA testing are now in widespread use, a functional automatic inspection system is becoming essential and urgent for its clinical application.

An automatic inspection system for ANA testing can be divided into HEp-2 cell detection, fluorescence pattern classification and computer aided diagnosis phases. Perner et al. [6] proposed the mining knowledge for HEp-2 cell image classification, but the study only focused on HEp-2 cell classification. Sack et al. [7] also mainly focused on HEp-2 immunofluorescence patterns classification. This study used simple automatic threshold to segment the cells. Soda et al. [3] only proposed the classification schema algorithm for ANA imaging. The shortcoming of these studies is that they didn’t perform efficient segmentation methods to outline the cells in the ANA image. Hence this study focused on the first phase of cell detecting and locating.

An efficient segmentation method is proposed for automatically detecting cells with fluorescence pattern in IIF imaging. The preprocessing in the proposed method reduced the any amount of noises but preserves the shape and contrast of cells. Then a two-staged watershed transform automatically extracts outlines of cells from IIF images. The watershed transformation, which is a reliable unsupervised model, was applied to solve diverse image segmentation problems. The results of computer simulations revealed that the proposed method always identified cell outlines as were obtained by that of physician manual sketched. The proposed automatic segmentation system provides robust automatic segmentation of HEp-2 fluorescent patterns in ANA testing and can save much of the time required to locate fluorescence patterns with very high stability.

After the segmentation, this study proposed a classification scheme based on Learning Vector Quantization (LVQ) classifier with 51 features to identify fluorescence patterns. The features included standard deviation, uniformity and entropy, block variation of local correlation coefficients (BVLC), spatial gray-level dependence matrices (SGLDM), gray-level difference matrix (GLDM), neighborhood gray-tone difference matrix (NGTDM), fractal dimension and Image coarse degrees. The classification result is estimated with correct rate. The total average accuracy is 80.3%. The result shows that these features are useful for fluorescence pattern classification.

CHAPTER 2

MATERIALS AND METHODS

2.1 DATA ACQUISITION

This study used slides of HEp-2 substrate, at a serum dilution of 1:80. A physician takes images of slides with an acquisition unit consisting of the fluorescence microscope coupled with a commonly used fluorescence microscope (Axioskop 2, CarlZeiss, Jena, Germany) at 40-fold magnification. The immunofluorescence images were taken by an operator with a color digital camera (E-330, Olympus, Tokyo, Japan). The digitized images were of 8-bit photometric resolution for each RGB (Red, Green and Blue) color channel with a resolution of 3136×2352 pixel. Finally, the images were transferred to a personal computer and stored as *.orf-files (Raw data format) without compression. The image database containing 44 samples were collected from January 2007 to July 2007. Due to the size of original images was too large to adapt a segmentation procedure, thus this study down-sampled the image to a reasonable resolution 1024 × 768 pixel.

2.2 AUTOANTIBODY FLUORESCENCE PATTERNS

To evaluate the proposed system, the IIF image database included six primary ANA patterns: diffuse pattern, peripheral pattern, coarse speckled pattern, fine speckled pattern, discrete speckled pattern, and nucleolar pattern. Figures 1 illustrate the relation of the six main ANA patterns. If the ANA testing detected anyone of the six patterns, it could have some diseases on patients. For example, if it detected the coarse speckled pattern, the patients may have systemic lupus erythematosus (SLE), mixed connective tissue disease (MCTD), progressive systemic sclerosis (PSS) or

cryoglobulinemia. Systemic lupus erythematosus is a chronic autoimmune disease that can be fatal, though with recent medical advances, fatalities are becoming increasingly rare. As with other autoimmune diseases, the immune system attacks the body’s cells and tissue, resulting in inflammation and tissue damage. SLE can affect any part of the body, but most often harms the heart, joints, skin, lungs, blood vessels, liver, kidneys and nervous system. The course of the disease is unpredictable, with periods of illness alternating with remissions. Lupus can occur at any age, and is most common in women. Lupus is treatable symptomatically, mainly with corticosteroids and immunosuppressants, though there is currently no cure. Mixed connective tissue disease is a serious autoimmune disease, in which the body's defense system attacks itself. MCTD combines features of polymyositis, systemic lupus erythematosus, scleroderma, and dermatomyositis, and is thus considered an overlap syndrome. MCTD commonly causes swelling, malaise, Raynaud phenomenon, muscle inflammation, and sclerodactyly. Scleroderma is a chronic disease characterized by excessive deposits of collagen in the skin or other organs. The localized type of the disease, while disabling, tends not to be fatal. The systemic type or systemic sclerosis, the generalized type of the disease, can be fatal as a result of heart, kidney, lung or intestinal damage autoimmune disease. Progressive systemic sclerosis is the most severe form. It has a rapid onset, involves more widespread skin hardening, will generally cause much internal organ damage (specifically the lungs and gastrointestinal tract), and is generally more life threatening. Cryoglobulins are proteins that become insoluble at reduced temperatures- less than 4 degrees Celsius. Cryoglobulinaemia is the presence of large amounts of cryoglobulin in the blood. It can be associated with various diseases. Nucleolar pattern may have PSS. Discrete speckled pattern may have limited type PSS, primary biliary cirrhosis or pulmonary

hypertension. In typical cases of limited scleroderma, Raynaud's phenomenon may precede scleroderma by several years. Raynaud's phenomenon is due to vasoconstriction of the small arteries of exposed peripheries (particularly the hands and feet in the cold). It is classically characterised by a triphasic color change - first white, then blue and finally red on rewarming. The scleroderma may be limited to the fingers - known as sclerodactyly. The limited form is often referred to as CREST syndrome. "CREST" is an acronym for the five main features which are Calcinosis , Raynaud's syndrome, Esophageal dysmotility, Sclerodactyly and Telangiectasia. CREST is a limited form associated with antibodies against centromeres and usually spares the lungs and kidneys. Primary biliary cirrhosis is an autoimmune disease of the liver marked by the slow progressive destruction of the small bile ducts (bile canaliculi) within the liver. When these ducts are damaged, bile builds up in the liver (cholestasis) and over time damages the tissue. This can lead to scarring, fibrosis, cirrhosis, and ultimately liver failure. In medicine, pulmonary hypertension is an increase in blood pressure in the pulmonary artery, pulmonary vein, or pulmonary capillaries, together known as the lung vasculature, leading to shortness of breath, dizziness, fainting, and other symptoms, all of which are exacerbated by exertion. Pulmonary hypertension can be a severe disease with a markedly decreased exercise tolerance and heart failure. Peripheral pattern may have specific for SLE. Fine speckled pattern may have Sjögren's syndrome. Sjögren's syndrome is an autoimmune disorder in which immune cells attack and destroy the exocrine glands that produce tears and saliva. Sjögren's syndrome is also associated with rheumatic disorders such as rheumatoid arthritis. The hallmark symptoms of the disorder are dry mouth and dry eyes. In addition, Sjögren's syndrome may cause skin, nose, and vaginal dryness, and may affect other organs of the body, including the kidneys, blood vessels, lungs, liver,

pancreas, and brain. Finally, diffused pattern may have specific for SLE or drug-induced lupus erythematosus (DIL). Drug-induced lupus erythematosus is an autoimmune disorder, similar to SLE, which is induced by chronic use of certain drugs. These drugs cause an autoimmune response producing symptoms similar to those of SLE. Symptoms of drug-induced lupus erythematosus include joint pain, fever, inflammation of the heart and lungs, elevated blood pressure, skin rashes and anterior uveitis. These signs and symptoms are not side effects of the drugs taken which occur during short term use. DIL occurs over long-term and chronic use of the medications listed above. While these symptoms are similar to those of systemic lupus erythematosus, they are generally not as severe unless they are ignored which leads to more harsh symptoms, and in some reported cases, death.

Figures 2 illustrate the distinct autoantibody fluorescence patterns. In the view point of image segmentation, the fluorescence cell belongs to diffuse, peripheral, coarse speckled, or fine speckled pattern normally includes only one connected region. On the contrary, the discrete speckled and nucleolar patterns consist of mass and several connected regions, respectively. Hence the contouring the cells belonged to the discrete speckled and nucleolar patterns seem complicated than others.

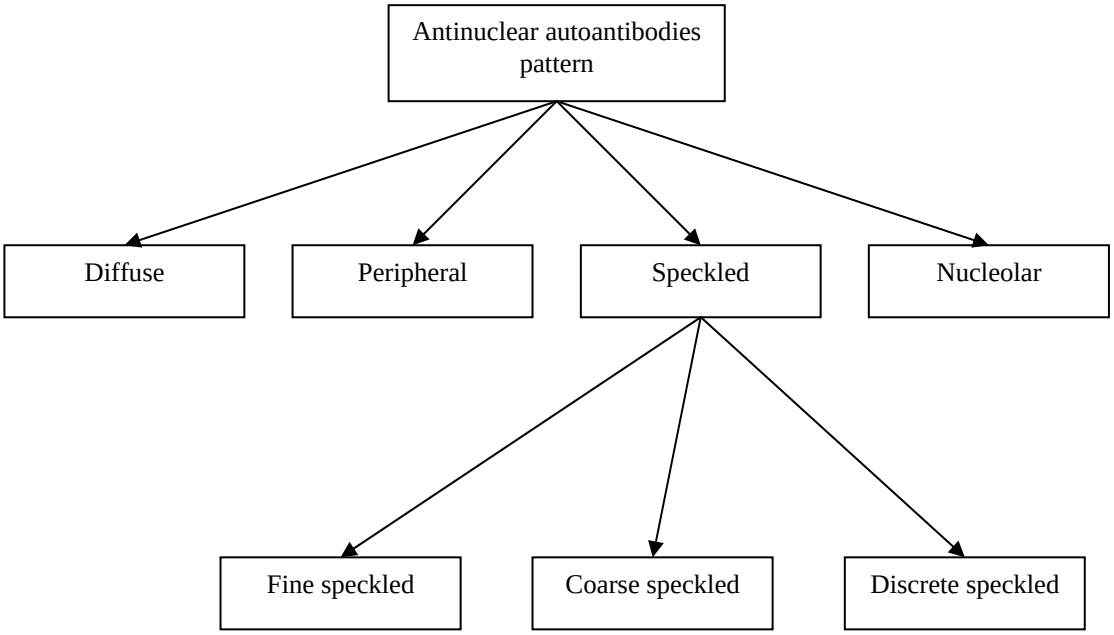

Fig. 1. The Antinuclear autoantibodies patterns

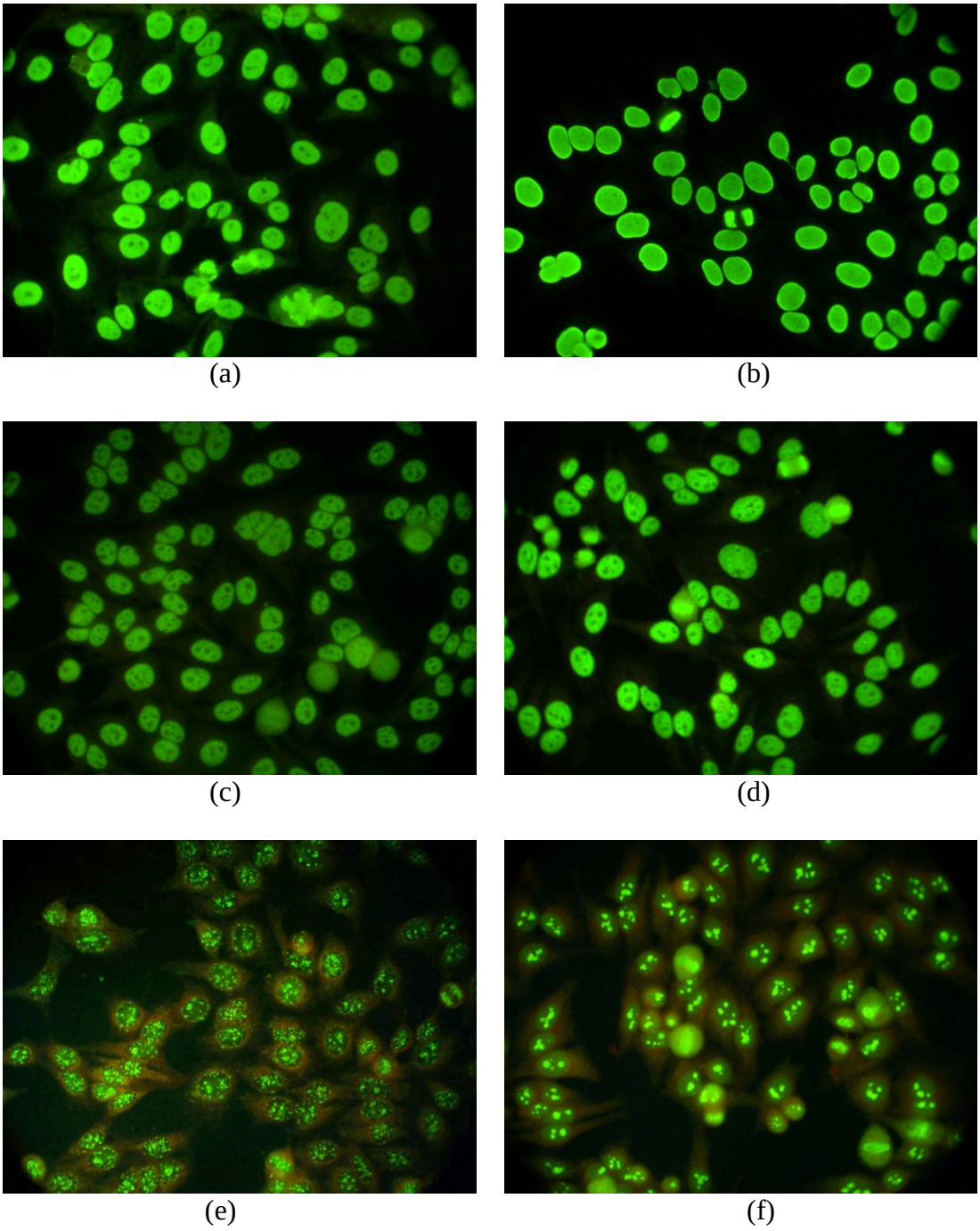

Fig. 2. The six distinct autoantibody fluorescence patterns: (a) diffuse, (b) peripheral, (c) coarse speckled, (d) fine speckled, (e) discrete speckled, and (f) nucleolar

2.3 TWO STAGED WATERSHED SEGMENTATION

The watershed transformation has been shown as one of the most reliable region-based methods of automatic and unsupervised segmentation [8]. This

technique has been applied successfully to solve a wide range of difficult problems of image segmentation [9-17]. In watershed transformation, a digital image was considered as the 3D topographic surfaces. The intensity of a pixel in the image denotes the elevation in the corresponding location. The objective of watershed transformation is to find the watershed lines in a topographic surface. However, the watershed transformation is sensitive to the noise and contrast in image. Over-segmentation may occur to generate incorrect outlines of fluorescence cells because IIF images always included noise and speckles. Thus preprocessing procedures were required for improving the performance of watershed segmentation. Besides, due to the variety of ANA patterns, the watershed transformation always failed to segment the cells with discrete speckled and nucleolar patterns. Accordingly, the proposed two-staged watershed segmentation was performed to obtain the precise outline of the cells. Figure 3 presents a flowchart of the proposed method, in the form included the first and second stage modules.

In the first stage segmentation, the green channel from the original RGB image was utilized as input intensity to segment cells. The median filter was performed to reduce noise and a common contrast adjustment was performed to enhance cell regions from background. For an image with L intensity levels, the original intensity $f(x, y)$ was transformed to the processed pixel intensity g(x, y) as

$$g(x, y) = \frac{f(x, y) - f_{\min}}{f_{\max} - f_{\min}} \times (L - 1), \quad (1)$$

where $f_{\min}$ and $f_{\max}$ are the minimal intensity and maximal intensity, respectively. After preprocessing, the proposed method employed the watershed transform to segment cell region. For reducing over-segmentation, the region merging procedure was utilized to merge the small connected regions. The region elimination procedure removed the segmented region with an unreasonable size (smaller than 100 pixels).

Then the first stage module counted the number of obtained cell (connected region)

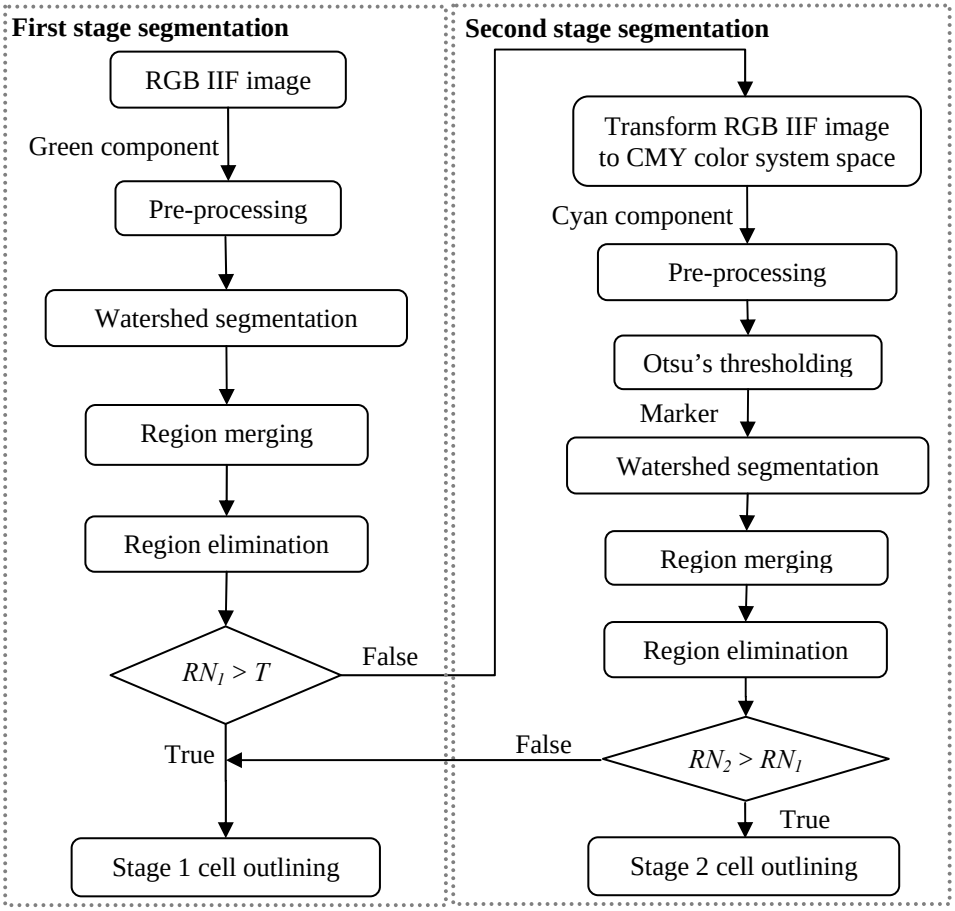

Fig. 3. The flowchart of the proposed two staged segmentation method

RN_1 in the image. The RN_1 was utilized to determine whether the image required the second stage segmentation or not. If RN_1 of an image was larger than a predefined threshold T, the segmentation result of the first stage module was approved and then generated the outline of cells. Figures 4 and Figures 5 demonstrate the results of the first stage module in the proposed method. On the contrary, if RN_1 was smaller than T, the first stage segmentation might obtain unsatisfied outline of cells due to the most cell regions were removed by the region elimination procedure. This situation was often seen in image with discrete speckled and nucleolar patterns. Thus the second stage segmentation was necessary for extracting the more precise cells.

In the second stage segmentation, the method based on the concept of markers was utilized for controlling over-segmentation. Lotufo and Falcao [18] proposed an algorithm for detecting watershed boundaries based on similarity using the markers. For the image with discrete speckled and nucleolar patterns, we found that the intensity dissimilarity between fluorescence cells and background was massive in the cyan component. Thus the second stage module utilized the cyan component as input to avoid over-segmentation. The original RGB image was transformed to CMY (Cyan, Magenta, and Yellow channels) color space [19]. The marker was defined as a connected component in image and typically select by a set of criteria from the pre-processed cyan component. In this work, the Otsu's algorithm [20] was first performed to generate the marker for watershed segmentation. The similarity-based watershed algorithm is performed herein to control over-segmentation in the images. Then the second stage module also calculated the number of obtained cell (connected region) RN_2 in the image. The segmentation result of the second stage module was approved and output the outline of cells when RN_2 was larger than RN_1. Figures 6 and Figures 7 show the outlining results by using the second stage module.

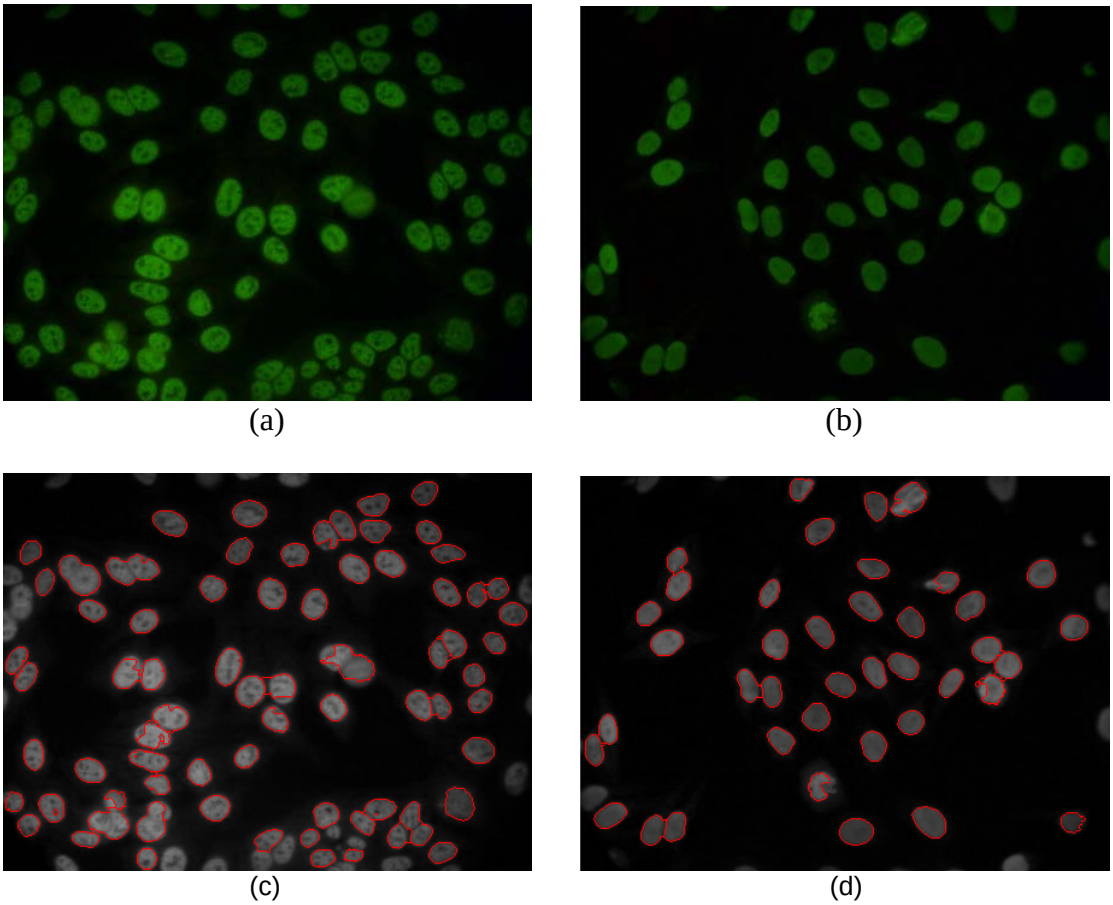

Fig. 4. IIF images segmented by the first stage module:(a) original RGB image with coarse speckled patterns, (b) image with diffuse patterns, (c) segmentation result of (a), and (d) segmentation result of (b)

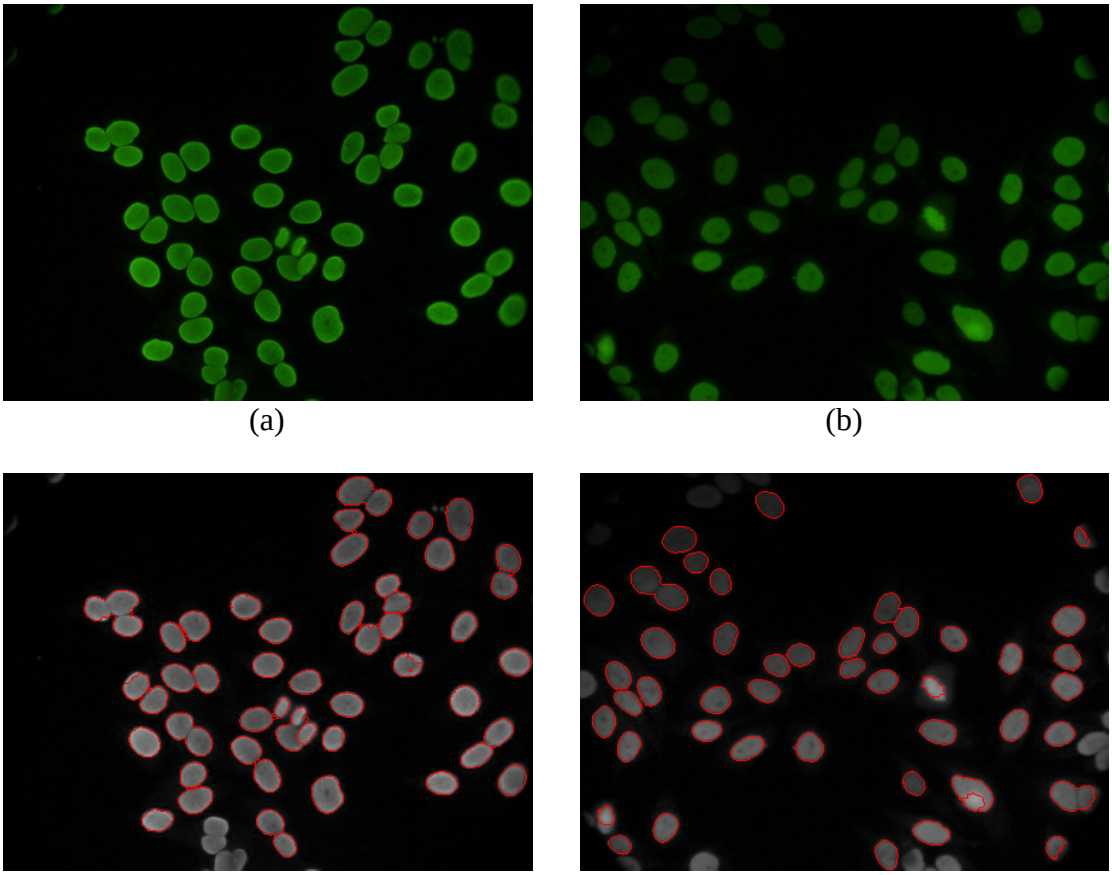

(a) (b)

(c) (d)

Fig. 5. IIF images segmented by the first stage module: (a) original RGB image with Peripheral patterns, (b) image with diffuse patterns, (c) segmentation result of (a), and (d) segmentation result of (b)

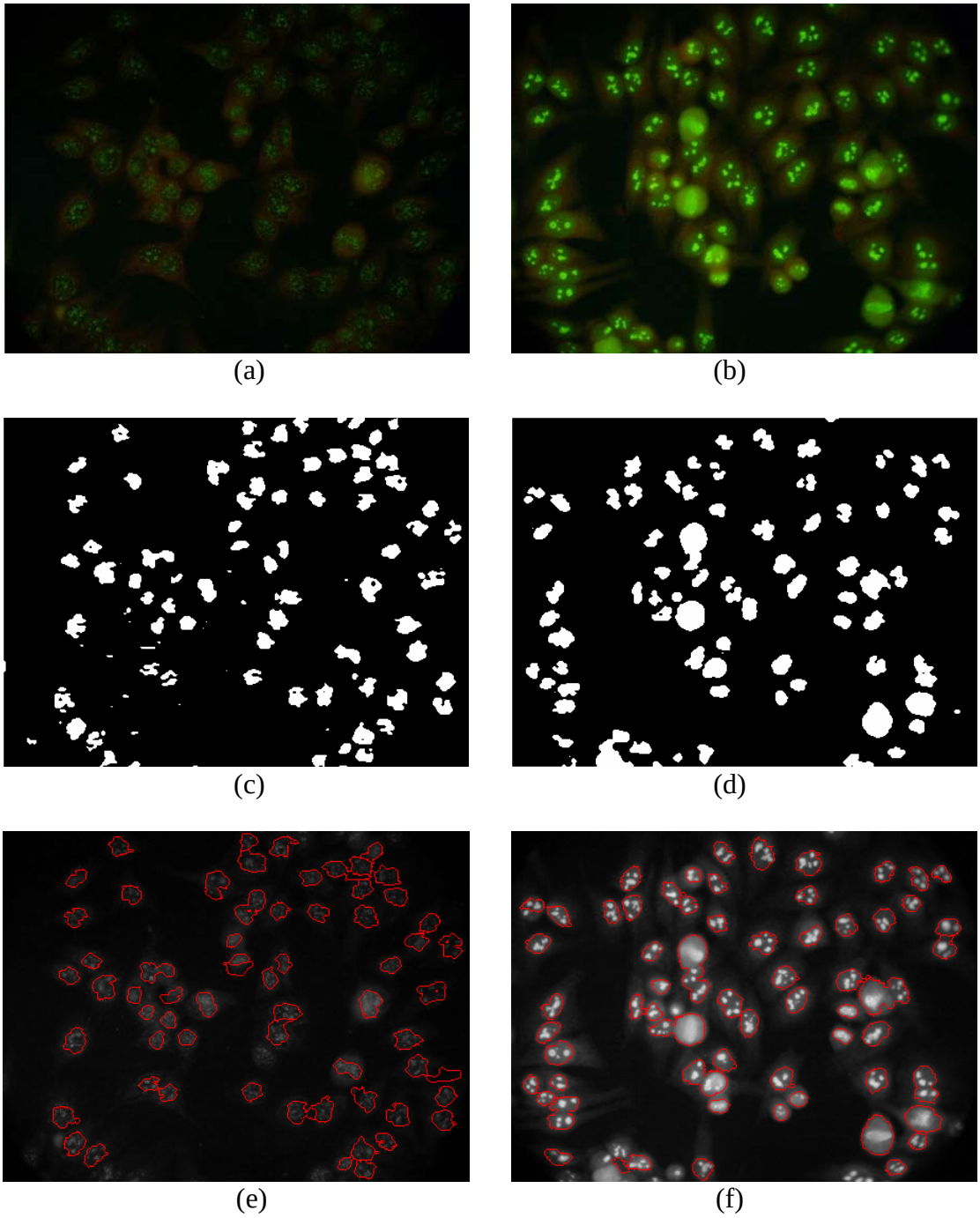

Fig. 6. IIF images processed with the second stage segmentation module: (a) original RGB image with discrete speckled patterns, (b) image with nucleolar patterns, (c) the marker of (a), (d) the marker of (b), (e) the cell outlining of (a), and (f) the cell outlining of (b)

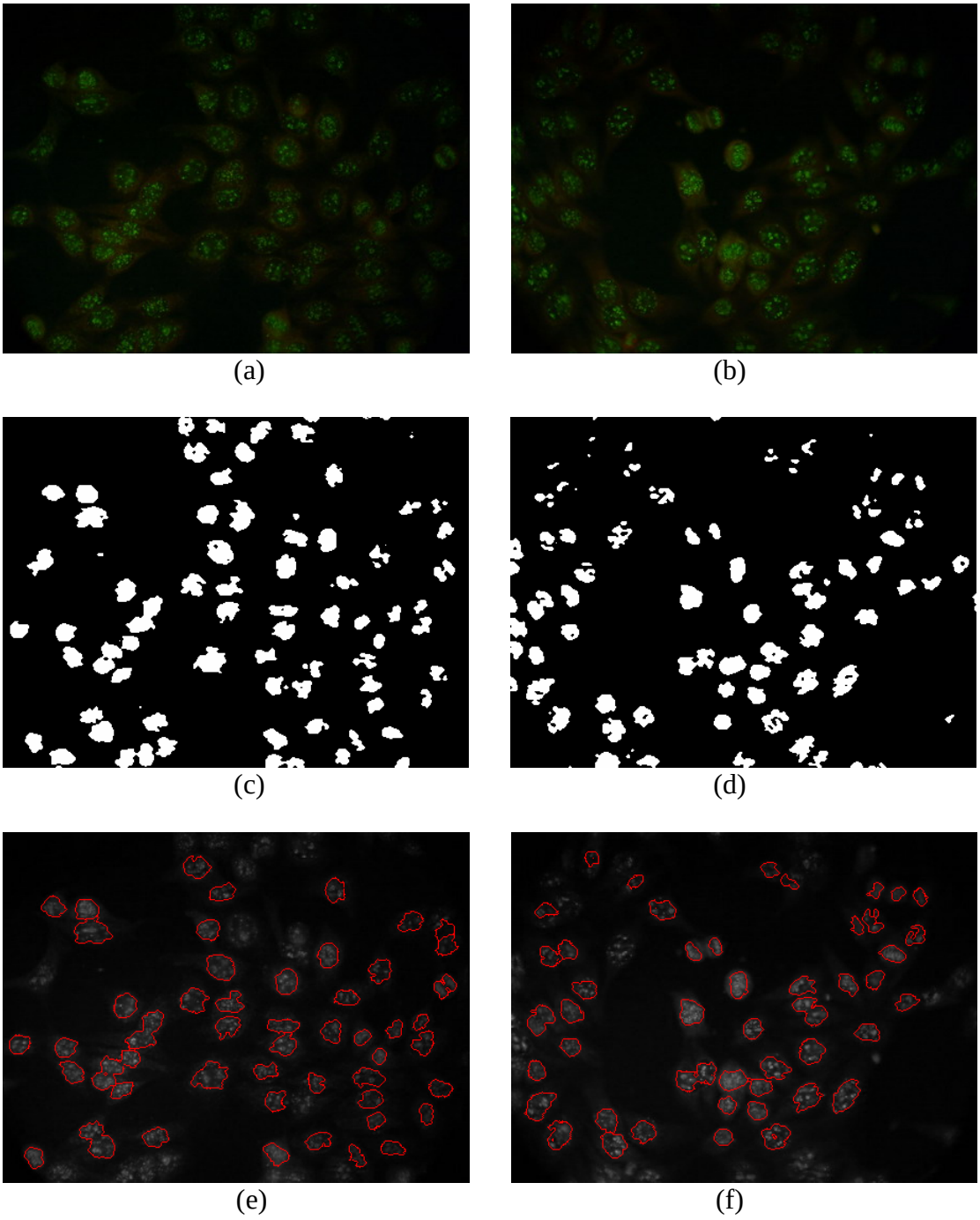

Fig. 7. IIF images processed with the second stage segmentation module: (a) original RGB image with discrete speckled patterns, (b) image with discrete speckled patterns, (c) the marker of (a), (d) the marker of (b), (e) the cell outlining of (a), and (f) the cell outlining of (b)

2.4 TEXTURE FEATURES ANALYSIS

Classification for HEp-2 cells can be divided into two parts. One is to find useful features which the differences between the six fluorescence patterns were the most. Another is how to choose a useful classifier. In this paper, totally 51 features utilized to identify fluorescence patterns, which were standard deviation, uniformity and entropy, block variation of local correlation coefficients (2 features), spatial gray-level dependence matrices (20 features), gray-level difference matrix (20 features), neighborhood gray-tone difference matrix (2 features), fractal dimension and image coarse degrees (3 features). The detailed description is given as follows.

2.4.1 STANDARD DEVIATION

In probability and statistics, the standard deviation is a measure of the dispersion of a set of values. It can apply to a probability distribution, a random variable, a population or a multi-set. The standard deviation is usually denoted with the letter σ. It is defined as the root-mean-square (RMS) deviation of the values from their mean, or as the square root of the variance. The standard deviation remains the most common measure of statistical dispersion, measuring how widely spread the values in a data set are. If many data points are close to the mean, then the standard deviation is small; if many data points are far from the mean, then the standard deviation is large. If all data values are equal, then the standard deviation is zero. A useful property of standard deviation is that, unlike variance, it is expressed in the same units as the data.

Equation (2) represents the mean value of image *I*, and Equation (3) represents the standard deviation value of image *I*, where *M* is the width of image *I* and *N* is the height of image *I*.

$$\bar{I} = \frac{1}{M \times N} \sum_{i=1}^{M} \sum_{j=1}^{N} I_{i,j} \tag{2}$$

$$\sigma = \sqrt{\frac{1}{M \times N} \sum_{i=1}^{M} \sum_{j=1}^{N} (I_{i,j} - \bar{I})} \tag{3}$$

2.4.2 UNIFORMITY AND ENTROPY

Some useful texture measures based on histograms include a measure of "Uniformity" given by equation (4) and an average "Entropy" measure, which is defined as equation (5), where z is a random variable denoting gray levels and $p(z_i)$, i = 0, 1, 2,…, L-1, is the corresponding histogram, L is the number of distinct gray levels. Because the p's have values in the range [0,1] and their sum equals 1, measure U is maximum for an image in which all gray levels are equal (maximally uniform), and decreases from there. Entropy is a measure of variability and is 0 for a constant image.

$$U = \sum_{i=0}^{L-1} p^2(z_i) \tag{4}$$

$$e = -\sum_{i=0}^{L-1} p(z_i) \log_2 p(z_i) \tag{5}$$

2.4.3 BLOCK VARIATION OF LOCAL CORRELATION COEFFICIENTS (BVLC)

The block variation of local correlation image is calculated from the equation (6) and (7):

$$\rho(k,l) = \frac{\frac{1}{M^2}\sum_{(i,j)\in B} I(i,j)I(i+k,j+l) - \mu_{0,0}\mu_{k,l}}{\sigma_{0,0}\sigma_{k,l}} \quad , \tag{6}$$

$$BVLC = \max_{(k,l)\in O_4}[\rho(k,l)] - \min_{(k,l)\in O_4}[\rho(k,l)], \qquad O_4 = \{(0,1),(1,0),(1,1),(1,-1)\}, \tag{7}$$

where $\mu_{0,0}$ and $\sigma_{0,0}$ are the local mean and standard deviation of the block with size $M \times M$. The (k, l) term denotes four shift directions, they are -90^o, 0 ^{o}, -45 ^{o}, 45 ^{o} respectively. The $\mu_{k,l}$ and $\sigma_{k,l}$ are the mean and standard deviation of the shifted block. The larger BVLC value means that the ingredients in the block are rough.

2.4.4 SPATIAL GRAY-LEVEL DEPENDENCE MATRICES (SGLDM)

The estimation of second-order conditional probability density functions are the main procedure of SGLDM. The second-order conditional probability density functions are denoted by $f(i, j \mid d, \theta)$. Here $f(i, j \mid d, \theta)$ is the probability function that records the count of the pixel pairs which separated by a distance d at an angle θ have gray levels i and j. The possible angle values are a multiple of 45 degrees. A total of 14 features can be extracted from the probability function $f(i, j \mid d, \theta)$. This study utilizes five of the 14 possible useful features, i.e. energy E, entropy H, correlation C, inertia I_n and local homogeneity L [21].

$$E = \sum_i \sum_j [S(i, j \mid d)^2], \tag{8}$$

$$H = -\sum_i \sum_j \theta(i, j \mid d) \log S_\theta(i, j \mid d), \tag{9}$$

$$C = {}^{1}\!/_{\sigma_x \sigma_y} \sum_i \sum_j (i - \mu_x)(j - \mu_y) S_\theta(i, j \mid d), \tag{10}$$

$$I_n = \sum_i \sum_j (i - j)^2 S_\theta(i, j \mid d), \tag{11}$$

$$L = \sum_i \sum_j \frac{1}{1+(i-j)^2} S_\theta(i, j \mid d), \tag{12}$$

where

$$\mu_x = \sum_i \sum_j S_\theta(i, j \mid d), \tag{13}$$

$$\sigma_x^2 = \sum_i (i - \mu_x)^2 \sum_j [S_\theta(i, j \mid d)], \tag{14}$$

where $S_\theta(i, j \mid d)$ is the $(i, j)^{\text{th}}$ element of S_θ when distance is d. The ranges of two summations are $i, j \in (0, N_G - 1)$ where N_G is the Maximum gray level value and $S_{\theta^0}(d) = f(i, j \mid d, \theta^o)$.

2.4.5 GRAY-LEVEL DIFFERENCE MATRIX (GLDM)

Digital gray-scaled images can be represented as a function of intensity and coordinate $I(x, y)$. Let $I_\sigma(x, y) = |I(x, y) - I(x + \Delta x, y + \Delta y)|$ for any given displacement $\sigma = (\Delta x, \Delta y)$ and $f'(i \mid \sigma)$ is the probability function of $I_\sigma(x, y)$. The possible values of $\sigma = (\Delta x, \Delta y)$ have the following forms: (0, d), (-d, d), (d, 0) and (-d, -d) where d is the displacement between pixel x and y. Five features are used in this study, i.e. contrast (*CON*), mean (*MEAN*), entropy (*ENT*), inverse difference moment (*IDM*) and angular second moment (*ASM*). The definitions of the five features are given as

$$CON = \sum_i i^2 f'(i \mid \sigma), \tag{15}$$

$$MEAN = \sum_i i f'(i \mid \sigma), \tag{16}$$

$$ENT = \sum_i f'(i \mid \sigma) \log(f'(i \mid \sigma)), \tag{17}$$

$$IDM = \sum_i f'(i \mid \sigma) \Big/ (i^2 + 1), \tag{18}$$

$$ASM = \sum_i [f'(i \mid \sigma)]^2 , \tag{19}$$

where $i \in (0, N_G - 1)$ and N_G is the Maximum gray level value just like in SGLDM.

2.4.6 NEIGHBORHOOD GRAY-TONE DIFFERENCE MATRIX (NGTDM)

The neighborhood gray-tone difference matrix is a column matrix estimated by equation (20) and (21). The estimated matrix is corresponding to the visual properties of an image.

$$\overline{A}_i = \overline{A}(k,l) = \frac{\sum_{m=-d}^{d} \sum_{n=-d}^{d} f(k+m, l+n)}{(2d+1)^2 - 1}, (m,n) \neq (0,0), \tag{20}$$

$$s(i) = \begin{cases} \sum \left| i - \overline{A}_i \right|, i \in N_i, N_i \neq \text{Ø} \\ 0 \qquad , otherwise \end{cases}, \tag{21}$$

where N_i is the set of all pixels having gray tone i (excluding the peripheral regions of width d). The mean and standard deviation value of the column matrix are calculated as the features used in the experiments.

2.4.7 FRACTAL DIMENSION

In fractal geometry [23], the fractal dimension, D, is a statistical quantity that gives an indication of how completely a fractal appears to fill space, as one zooms down to finer and finer scales. There are many specific definitions of fractal dimension and none of them should be treated as the universal one. From the theoretical point of view the most important are the Hausdorff dimension [24], the

packing dimension. On the other hand the box-counting dimension and correlation dimension are widely used in practice, partly due to their ease of implementation. Although for some classical fractals all these dimensions do coincide, in general they are not equivalent. For example, what is the dimension of the Koch snowflake? It has topological dimension one, but it is by no means a curve the length of the curve between any two points on it is infinite. No small piece of it is line-like, but neither is it like a piece of the plane or any other. In some sense, we could say that it is too big to be thought of as a one-dimensional object, but too thin to be a two-dimensional object, leading to the question of whether its dimension might best be described in some sense by number between one and two. This is just one simple way of motivating the idea of fractal dimension.

There are two main approaches to generate a fractal structure. One is growing from a unit object, and the other is to construct the subsequent divisions of an original structure, like the Sierpinski triangle (Figure 8).

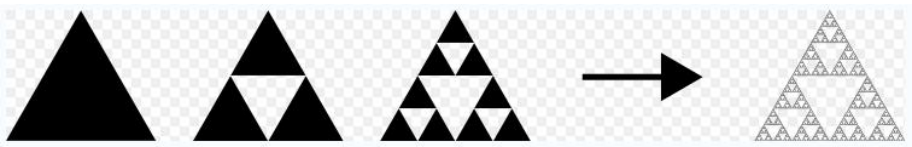

Fig. 8. Sierpinski triangle

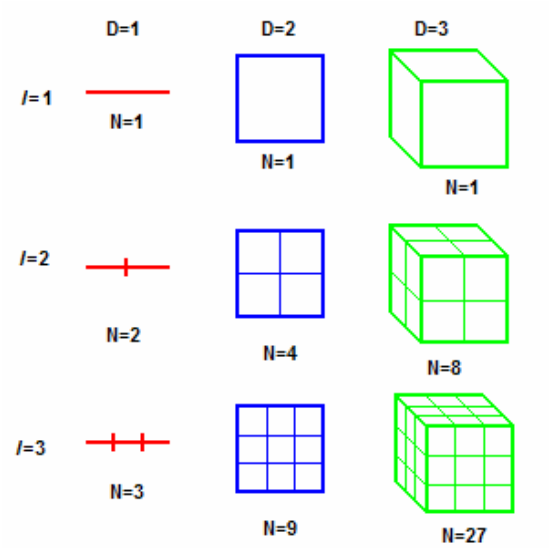

Fig. 9. Another way to define dimension

Here we follow the second approach to define the dimension of fractal structures. If we take an object with linear size equal to 1 residing in Euclidean dimension, and reduce its linear size to be l in each spatial direction, it takes $N(1)$ number of self similar objects to cover the original object (Figure 9). However, the dimension defined by

$$D = \frac{\log N(l)}{\log \frac{1}{l}} \tag{22}$$

is still equal to its topological or Euclidean dimension. By applying the above equation to fractal structure, we can get the dimension of fractal structure (which is more or less the Hausdorff dimension) as a non-whole number as expected.

$$D = \lim_{\varepsilon \to 0} \frac{\log N(\varepsilon)}{\log \frac{1}{\varepsilon}} \tag{23}$$

2.4.8 IMAGE COARSE DEGREES

In this paper, we use a method to find image coarse degrees for classification. It explains as follows. Only consider the relative relation between pixels and its neighbor pixels in images. Because relations are restricted to the pixels permutation way in digital images, so it can to divide into four directions in general. The inequalities (a) to (h) show the eight coarse point conditions. When pixel in image was satisfied the any one eight conditions, the pixel was considered as a coarse point. Then, let $W(x, y) = 1$. But when it was not satisfied the any one eight conditions, let $W(x, y) = 0$. By checking (a) to (h), it can find the all coarse points in image.

Maxima: $s(x, y) > \max[s(x+1, y), s(x-1, y)]$ (a)

$s(x, y) > \max[s(x, y+1), s(x, y-1)]$ (b)

$s(x, y) > \max[s(x+1, y+1), s(x-1, y-1)]$ (c)

$s(x, y) > \max[s(x+1, y-1), s(x-1, y+1)]$ (d)

Minima: $s(x, y) < \max[s(x+1, y), s(x-1, y)]$ (e)

$s(x, y) < \max[s(x, y+1), s(x, y-1)]$ (f)

$s(x, y) < \max[s(x+1, y+1), s(x-1, y-1)]$ (g)

$s(x, y) < \max[s(x+1, y-1), s(x-1, y+1)]$ (h)

Then, using equation (24) to count how many coarse points in the image and obtain the average coarse degrees R_m.

$$R_m = \frac{1}{N^2} \sum_{x=0}^{N-1} \sum_{y=0}^{N-1} W(x, y) \tag{24}$$

Usually, blocks in image may have different coarse degrees. In other words, some blocks may smooth and some blocks may rough in one image. So, even the average coarse degree was the same in two images, but may means different meaning.

W_{11}	W_{12}	W_{13}	W_{14}
W_{21}	W_{22}	W_{23}	W_{24}
W_{31}	W_{32}	W_{33}	W_{34}
W_{41}	W_{42}	W_{43}	W_{44}

Fig. 10. Blocks coarse degree in image

First, image was divided into some number blocks. And to count each total coarse points in each blocks. If each block was sized $n \times n$, then the equation (25) can calculate the coarse degree standard deviation R_{sd}, where $\overline{w}$ is the average of w_{ij}. The entropy of these coarse degrees R_{en} is equation (26). R_{sd} and R_{en} can represent the more difference between images.

$$R_{sd} = \frac{1}{n^2}\sqrt{\sum_{x=1}^{n}\sum_{y=1}^{n}\left|w_{ij} - \overline{w}\right|^2} \tag{25}$$

$$R_{en} = \frac{-1}{n^2}\sum_{x=1}^{n}\sum_{y=1}^{n} w_{i,j} \times \log(w_{i,j}) \tag{26}$$

2.5 LEARNING VECTOR QUANTIZATION (LVQ)

Learning vector quantization (LVQ), is a prototype-based supervised classification algorithm. LVQ can be understood as a special case of an artificial neural network, more precisely, it applies a winner-take-all Hebbian learning-based approach. It is a precursor to self-organizing maps (SOM) and related to Neural gas, and to the k-Nearest Neighbor algorithm (k-NN). LVQ was invented by Teuvo Kohonen. The network has two layers: a layer of input neurons, and a layer of output neurons. The network is given by prototypes $W = (w(i),...,w(n))$. It changes the weights of the network in order to classify the data correctly. For each data point, the prototype (neuron) that is closest to it is determined (called the winner neuron). The weights of the connections to this neuron are then adapted, i.e. made closer if it correctly classifies the data point or made less similar if it incorrectly classifies it. An advantage of LVQ is that it creates prototypes that are easy to interpret for experts in the field. LVQ can be a source of great help in classifying text documents.

CHAPTER 3

RESULTS

3.1 SEGMENTATION RESULTS

This study totally experimented 2305 autoantibody fluorescence patterns (including 456 diffuse patterns, 417 peripheral patterns, 719 coarse speckled patterns, 55 fine speckled patterns, 517discrete speckled patterns and 141 nucleolar patterns) with manual sketched outlines from 44 IIF images to test the accuracy of the proposed method. The simulations were made on a single CPU Intel Pentium-VI 3.0 GHz personal computer with Microsoft Windows XP operating system.

In this study, the preprocessing procedure utilized the sized 3 × 3 median filter to reduce noise. In the first stage segmentation, the predefined threshold T for RN1 ranged from 20 to 30, the proposed system obtained a stable and the highest accuracy. The performance measures, i.e. true-positive (TP), false-negative (FN), false-positive (FP) and sensitivity, were used to estimate the performance of the proposed system. The TP value denotes the number of correct segmented cells; FN value denotes the number of missed cells; FP value denotes the number of incorrect segmented region without any fluorescence cell; and the sensitivity is defined as TP / (TP+FN). Table 1 lists the segmentation results of the proposed method. From the segmentation results, only a small number of cases might generate an undesired segmentation. Table 1 lists the segmentation results of the proposed method. The sensitivity of the discrete speckled pattern was 86.8%, others were from 94.7% to 100%. The total average sensitivity was 94.7%. From the segmentation results, only a small number of cases might generate an undesired segmentation.

Table 1. Fluorescence patterns segmentation results of the proposed method

Autoantibody fluorescence pattern(number of slices)	TP	FP	FN	Sensitivity (%)
Diffused (10)	449	1	7	98.5%
Peripheral (10)	411	0	6	98.6%
Coarse speckled (10)	681	2	38	94.7%
Fine speckled (1)	55	0	0	100%
Discrete speckled (10)	449	5	68	86.8%
Nucleolar (3)	138	0	3	97.9%
Total	2183	8	122	94.7%

TP = true-positive;
FN = false-negative;
FP = false-positive;
Sensitivity = TP / (TP+FN)

3.2 CLASSIFICATION RESULTS

This study totally experimented on 1036 autoantibody fluorescence patterns from the segmentation results. Table 2 shows the information of training data and testing data. There are 782 cells in training data and 254 cells in testing data.

First, only the green channel from training data utilized as input intensity for texture analysis. Second, calculate the standard deviation, uniformity and entropy, BVLC, SGLDM, GLDM, NGTDM, fractal dimension and image coarse degrees to obtain the 51 features. Third, because each value of the 51 features is vary different. Some values may vary large and some values may vary small. Due to the large value of the features may reduce the small value of the features for the influence of classification. This may cause the bad classification result. So, these values of the features must be normalized. Normalization utilized the equation (27) to obtain new value $x_{ij}^{'}$, where i represent the ith cell and j represent the jth feature.

These new values of the features after normalization are [0, 1]. Figure 11 represent the original values. From this figure, it can easily find that some values are large and some are smaller than the large value. Figure 12 represent the new values after the normalization. From this figure, it can find that no matter these large or small values are between [0, 1].

Table 2. The samples in the training set and in the testing set

fluorescence patterns	Training data	Testing data
Coarse speckled	150	62
Diffuse	115	38
Discrete speckled	118	37
Fine speckled	148	37
Nucleolar	124	40
Peripheral	127	40
Total	782	254

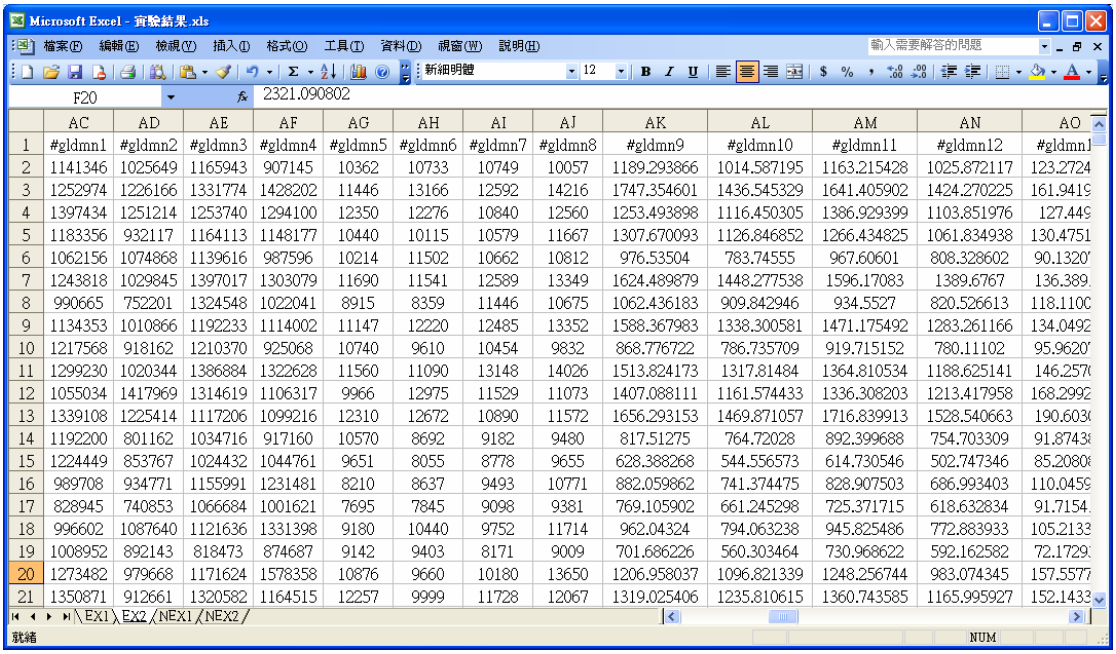

	AC	AD	AE	AF	AG	AH	AI	AJ	AK	AL	AM	AN	AO
1	#gldmn1	#gldmn2	#gldmn3	#gldmn4	#gldmn5	#gldmn6	#gldmn7	#gldmn8	#gldmn9	#gldmn10	#gldmn11	#gldmn12	#gldmn1
2	1141346	1025649	1165943	907145	10362	10733	10749	10057	1189.293866	1014.587195	1163.215428	1025.872117	123.2724
3	1252974	1226166	1331774	1428202	11446	13166	12592	14216	1747.354601	1436.545329	1641.405902	1424.270225	161.9419
4	1397434	1251214	1253740	1294100	12350	12276	10840	12560	1253.493898	1116.450305	1386.929399	1103.851976	127.449
5	1183356	932117	1164113	1148177	10440	10115	10579	11667	1307.670093	1126.846852	1266.434825	1061.834938	130.4751
6	1062156	1074868	1139616	987596	10214	11502	10662	10812	976.53504	783.74555	967.60601	808.328602	90.1320
7	1243818	1029845	1397017	1303079	11690	11541	12589	13349	1624.489879	1448.277538	1596.17083	1389.6767	136.389
8	990665	752201	1324548	1022041	8915	8359	11446	10675	1062.436183	909.842946	934.5527	820.526613	118.1100
9	1134353	1010866	1192233	1114002	11147	12220	12485	13352	1588.367983	1338.300581	1471.175492	1283.261166	134.0492
10	1217568	918162	1210370	925068	10740	9610	10454	9832	868.776722	786.735709	919.715152	780.11102	95.9620
11	1299230	1020344	1386884	1322628	11560	11090	13148	14026	1513.824173	1317.81484	1364.810534	1188.625141	146.257
12	1055034	1417969	1314619	1106317	9966	12975	11529	11073	1407.088111	1161.574433	1336.308203	1213.417958	168.2992
13	1339108	1225414	1117206	1099216	12310	12672	10890	11572	1656.293153	1469.871057	1716.839913	1528.540663	190.603
14	1192200	801162	1034716	917160	10570	8692	9182	9480	817.51275	764.72028	892.399688	754.703309	91.8743
15	1224449	853767	1024432	1044761	9651	8055	8778	9655	628.388268	544.556573	614.730546	502.747346	85.2080
16	989708	934771	1155991	1231481	8210	8637	9493	10771	882.059862	741.374475	828.907503	686.993403	110.0459
17	828945	740853	1066684	1001621	7695	7845	9098	9381	769.105902	661.245298	725.371715	618.632834	91.7154
18	996602	1087640	1121636	1331398	9180	10440	9752	11714	962.04324	794.063238	945.825486	772.883933	105.2133
19	1008952	892143	818473	874687	9142	9403	8171	9009	701.686226	560.303464	730.968622	592.162582	72.1729
20	1273482	979668	1171624	1578358	10876	9660	10180	13650	1206.958037	1096.821339	1248.256744	983.074345	157.5577
21	1350871	912661	1320582	1164515	12257	9999	11728	12067	1319.025406	1235.810615	1360.743585	1165.995927	152.1433

Fig. 11. The original values of 51 features

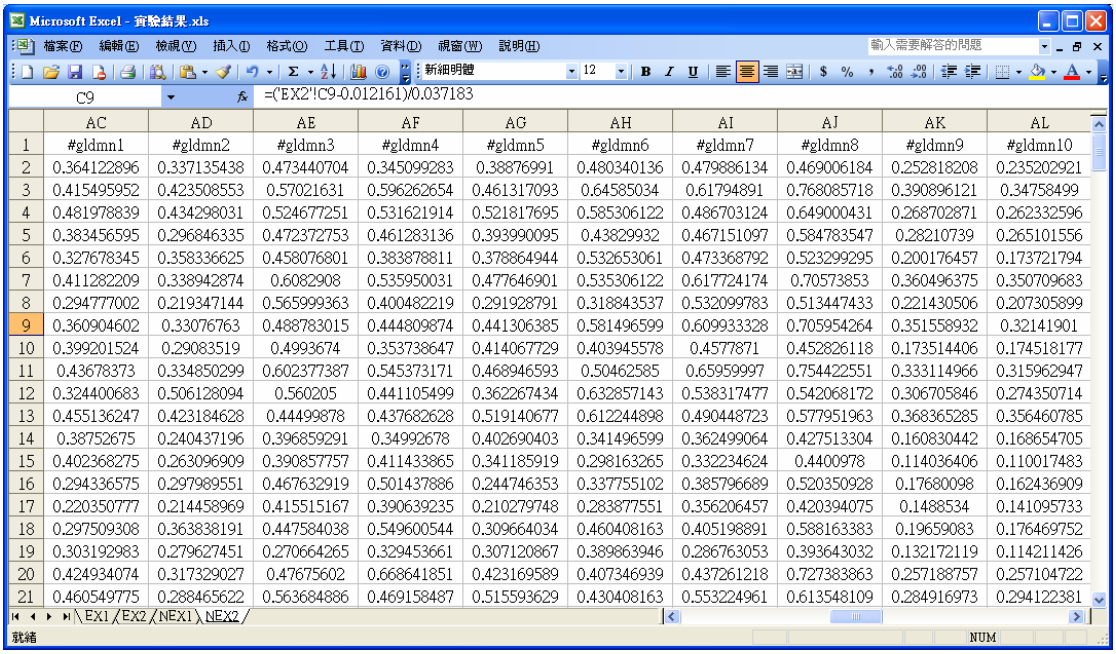

	AC	AD	AE	AF	AG	AH	AI	AJ	AK	AL
1	#gldmn1	#gldmn2	#gldmn3	#gldmn4	#gldmn5	#gldmn6	#gldmn7	#gldmn8	#gldmn9	#gldmn10
2	0.364122896	0.337135438	0.473440704	0.345099283	0.38876991	0.480340136	0.479886134	0.469006184	0.252818208	0.235202921
3	0.415495952	0.423508553	0.57021631	0.596262654	0.461317093	0.64585034	0.61794891	0.768085718	0.390896121	0.34758499
4	0.481978839	0.434298031	0.524677251	0.531621914	0.521817695	0.585306122	0.486703124	0.649000431	0.268702871	0.262332596
5	0.383456595	0.296846335	0.472372753	0.461283136	0.393990095	0.43829932	0.467151097	0.584783547	0.28210739	0.265101556
6	0.327678345	0.358336625	0.458076801	0.383878811	0.378864944	0.532653061	0.473368792	0.523299295	0.200176457	0.173721794
7	0.411282209	0.338942874	0.6082908	0.535950031	0.477646901	0.535306122	0.617724174	0.70573853	0.360496375	0.350709683
8	0.294777002	0.219347144	0.565999363	0.400482219	0.291928791	0.318843537	0.532099783	0.513447433	0.221430506	0.207305899
9	0.360904602	0.33076763	0.488783015	0.444809874	0.441306385	0.581496599	0.609933328	0.705954264	0.351558932	0.32141901
10	0.399201524	0.29083519	0.4993674	0.353738647	0.414067729	0.403945578	0.4577871	0.452826118	0.173514406	0.174518177
11	0.43678373	0.334850299	0.602377387	0.545373171	0.468946593	0.50462585	0.65959997	0.754422551	0.333114966	0.315962947
12	0.324400683	0.506128094	0.560205	0.441105499	0.362267434	0.632857143	0.538317477	0.542068172	0.306705846	0.274350714
13	0.455136247	0.423184628	0.44499878	0.437682628	0.519140677	0.612244898	0.490448723	0.577951963	0.368365285	0.356460785
14	0.38752675	0.240437196	0.396859291	0.34992678	0.402690403	0.341496599	0.362499064	0.427513304	0.160830442	0.168654705
15	0.402368275	0.263096909	0.390857757	0.411433865	0.341185919	0.298163265	0.332234624	0.4400978	0.114036406	0.110017483
16	0.294336575	0.297989551	0.467632919	0.501437886	0.244746353	0.337755102	0.385796689	0.520350928	0.17680098	0.162436909
17	0.220350777	0.214458969	0.415515167	0.390639235	0.210279748	0.283877551	0.356206457	0.420394075	0.1488534	0.141095733
18	0.297509308	0.363838191	0.447584038	0.549600544	0.309664034	0.460408163	0.405198891	0.588163383	0.19659083	0.176469752
19	0.303192983	0.279627451	0.270664265	0.329453661	0.307120867	0.389863946	0.286763053	0.393643032	0.132172119	0.114211426
20	0.424934074	0.317329027	0.47675602	0.668641851	0.423169589	0.407346939	0.437261218	0.727383863	0.257188757	0.257104722
21	0.460549775	0.288465622	0.563684886	0.469158487	0.515593629	0.430408163	0.553224961	0.613548109	0.284916973	0.294122381

Fig. 12. The new values of 51 features after the normalization

Fourth, it utilized LVQ with these new values of the 51 features to train. After the training, repeat the above-mentioned steps for the testing. Finally, the testing result was produced. Table 3 show the classification result of the LVQ with 51 features. In these six patterns, the correct rate of fine speckled pattern is the best which is 0.892. The correct rate of coarse speckled and nucleolar pattern are larger than 0.8. The worst value of the correct rate is 0.7, which is peripheral pattern. The total average correct rate is 0.803.

$$x_{ij}^{'} = \frac{x_{ij} - x_{j\min}}{x_{j\max} - x_{j\min}} \tag{27}$$

$$x_{j\max} = \max(x_{1j}, x_{2j}, \ldots, x_{nj}) \tag{28}$$

$$x_{j\min} = \min(x_{1j}, x_{2j}, \ldots, x_{nj}) \tag{29}$$

Table 3. The simulation result of the LVQ model with 51 features

	Number(*N*)	Correct Number(*CN*)	Correct Rate(*CN*/*N*)
Coarse speckled	62	55	0.887
Diffuse	38	27	0.711
Discrete speckled	37	28	0.757
Fine speckled	37	33	0.892
Nucleolar	40	33	0.825
Peripheral	40	28	0.7
Total	254	204	0.803

CHAPTER 4

CONCLUSION

This thesis presented a two-staged segmentation method for automatically detecting outlines of fluorescence cells in IIF images. The preprocessing filter and enhancement were utilized for the first stage watershed algorithm automatically produces the outline of the cell. In the second stage segmentation, the similarity-based watershed algorithm performed the marker to prevent over-segmentation. The IIF image database including 2305 fluorescence cells were used to evaluate the performance of the proposed segmentation scheme. From the simulation results, the proposed method determines the outlines of cells that are very similar to manual sketched ones. The results revealed that the proposed method can practically outline fluorescence cells from IIF images. The results show that the watershed segmentation method is suit for outline detection for the HEp-2 cell in IIF images. But watershed segmentation usually caused over-segmentation results. So how to reduce over-segmentation results is a key point. In this study, the pre-processing, the region merging, the region elimination and the marker were be used to reduce over-segmentation results. By the proposed method, as long as the methods for reducing over-segmentation results can be improved, and the segmentation results can be better. Even the discrete speckled pattern was 86.8% also can get a better result from this method.

This study also proposed a classification method based on LVQ classifier with 51 features. These features are standard deviation, uniformity and entropy (2 features), BVLC (2 features), SGLDM (20 features), GLDM (20 features), NGTDM (2 features), Fractal dimension and Image coarse degrees (3 features). It totally experimented on

1036 (training data is 782 and testing data is 254) autoantibody fluorescence patterns from the segmentation results. The estimation of the classification result is correct rate. The total average correct rate is 0.803. In the six different patterns, the correct rate of the coarse speckled pattern is 0.887, the correct rate of the diffuse pattern is 0.711, the correct rate of the discrete speckled pattern is 0.757, the correct rate of the fine speckled pattern is 0.892, the correct rate of the nucleolar pattern is 0.825 and the correct rate of the peripheral pattern is 0.7. All the correct rate of the six patterns is larger than 0.7 or equal to 0.7. This result is not bad. By the results, it can be found that the 51 features are useful for classification with LVQ classifier.

References

[1] Conrad K, Schoessler W, and Hiepe F, *Autoantibodies in systemic autoimmune diseases* Pabst Science Publishers, 2002.

[2] Y.POLOTSKY, J.P.NATARO, D.KOTLER, T.J.BARRETT, and J.M.ORENSTEIN, "HEp-2 Cell Adherence Patterns, Serotyping, and DNA Analysis of Escherichia coli Isolates from Eight Patients with AIDS and Chronic Diarrhea," *JOURNAL OF CLINICAL MICROBIOLOGY*, pp. 1952-1958, 1997.

[3] Soda, Paolo, Iannello, and Giulio, "A Hybrid Multi-Expert Systems for HEp-2 Staining Pattern Classification," *Image Analysis and Processing*, pp. 685-690, 2007.

[4] Soda and Paolo, "Early Experiences in the Staining Pattern Classification of HEp-2 Slides," *Computer-Based Medical Systems*, pp. 219-224, 2007.

[5] Conrad K, Humbel RL, Meurer M, and Shoenfeld Y, *Autoantigens and autoantibodies: diagnostic tools and clues to understanding autoimmunity* Pabst Science Publishers, 2000.

[6] P. Perner, H. Perner, and B. Muller, "Mining knowledge for HEp-2 cell image classification," *Artificial Intelligence in Medicine*, vol. 26, no. 1-2, pp. 161-173, Sept. 2002.

[7] U. Sack, S. Knoechner, H. Warschkau, U. Pigla, F. Emmrich, and M. Kamprad, "Computer-assisted classification of HEp-2 immunofluorescence patterns in autoimmune diagnostics," *Autoimmunity Reviews*, vol. 2, no. 5, pp. 298-304, Sept. 2003.

[8] L. Vincent and P. Soille, "Watersheds in Digital Spaces - An Efficient Algorithm Based on Immersion Simulations," *Ieee Transactions on Pattern Analysis and Machine Intelligence*, vol. 13, no. 6, pp. 583-598, June 1991.

[9] Yi-Ying Wang, Yung-Nien Sun, Chou-Ching K.Lin, and Ming-Shaung Ju, "Nerve Cell Segmentation via Multi-Scale Gradient Watershed Hierarchies," *Engineering in Medicine and Biology Society*, pp. 4310-4313, Aug. 2006.

[10] Chen Jia-xin and Liu Sen, "A medical image segmentation method based on watershed transform," *Computer and Information Technology*, pp. 634-638, 2005.

[11] R.A. Lotufo, A.X. Falcao, and F.A. Zampirolli, "IFT-Watershed from gray-scale marker," *Computer Graphics and Image Processing*, pp. 146-152, 2002.

[12] J.M. Gauch, "Image Segmentation and Analysis via Multiscale Gradient Watershed Hierarchies," *Image Processing, IEEE Transactions*, vol. 8, no. 1, pp. 69-79, Jan. 1999.

[13] J.M. Gauch, "Image segmentation and analysis via multiscale gradient watershed hierarchies," *Ieee Transactions on Image Processing*, vol. 8, no. 1, pp. 69-79, Jan. 1999.

[14] F. Soares and F. Muge, "Watershed lines suppression by waterfall marker improvement and line-neighbourhood analysis," *Pattern Recognition*, vol. 1 pp. 604-607, 2004.

[15] P. Wang, X. Wu, and J. Tang, "Watershed Segmentation Based on Multiscale Morphological Fusion," *Signal Processing*, vol. 2 pp. 16-20, 2006.

[16] B. Deka and D. Ghosh, "Watershed Segmentation for Medical Ultrasound Images," *Systems, Man and Cybernetics*, vol. 4 pp. 3186-3191, Oct. 2006.

[17] A. Gouze, C. De Roover, B. Macq, A. Herbulot, E. Debreuve, and M. Barlaud, "Watershed-driven active contours for moving object segmentation," *Image Processing*, vol. 2 pp. II ?818, 2005.

[18] Lotufo R and Falcao A, "T*he ordered queue and the optimality of the watershed approaches,*" M*athematical Morphology and its Application to Image and Signal Processing,* pp. 341-450, 2000.

[19] Gonzalez RC and Woods RE., D*igital image processing. 2 ed.* Massachusetts: Addison Wesley, 2002.

[20] N. Otsu, "Threshold Selection Method from Gray-Level Histograms," I*eee Transactions on Systems Man and Cybernetics,* vol. 9, no. 1, pp. 62-66, 1979.

[21] V.N.Gudivada and V.V.Raghavan, "Content-Based Image Retrieval-Systems," C*omputer,* vol. 28 pp. 18-22, Sept. 1995.

[22] van der Sanden, J.J., and D.H.Hoekman, "Review of relationships between grey-tone co-occurrence, semivariance and autocorrelation based image texture analysis approaches," C*anadian Journal of Remote Sensing,* vol. 38 pp. 207-213, 2005.

[23] Mandelbrot B B, T*he Fractal Geometry of Nature* New York:W H Freeman and Company, 1982.

[24] M.Maurice Dodson and Simon Kristensen, "Hausdorff Dimension and Diophantine Approximation," P*roceedings of Symposia in Pure Mathematics,* June 2003.